Laser-Light Speckle Formation for Deflection-Shape Identification Using Digital Image Correlation

Klemen Zaletelj[a], Vid Agrež[a], Janko Slavič*[a], Rok Petkovšek[a], Miha Boltežar[a]

[a] *University of Ljubljana, Faculty of Mechanical Engineering, Aškerčeva 6, 1000 Ljubljana, Slovenia*

Cite as:
Klemen Zaletelj, Vid Agrež, Janko Slavič, Rok Petkovšek and Miha Boltežar, Laser-Light Speckle Formation for Deflection-Shape Identification Using Digital Image Correlation, Mechanical Systems and Signal Processing, Volume 161, December 2021, https://doi.org/10.1016/j.ymssp.2021.107899

Abstract

The application of a speckle pattern to the surface of a structure is usually required for Digital Image Correlation (DIC)-based displacement identification. A speckle pattern generally requires the modification (*e.g.*, painting) of the structure's surface.

An improved method of laser-light speckle formation for DIC measurement of relatively large structures is proposed, where the speckle pattern is formed by laser-light interference as a consequence of the surface roughness and the laser illumination, leaving the surface of the object untouched. The interference phenomena caused by the light reflecting from the rough surface create bright spots that move with the observed structure. The size of the speckles depends on the surface roughness, the experimental setup and the optical system. The proposed method is researched using three experimental cases: two rigid-body motion measurements and a full-field operating-deflection-shape measurement. The experiments show that motion can be identified even when the amplitudes of the oscillation are as low as $0.1\,\mu$m (on a scale of 1/1000 of a pixel).

While the laser speckle accuracy is promising, it was found to be less

*Corresponding author: janko.slavic@fs.uni-lj.si

accurate than painted speckle-pattern measurements, but with further development it could become a viable alternative.

Keywords: laser speckle, paint speckle, DIC, full-field vibration identification

1. Introduction

For measurements with a high spatial density, a large number of acceleration transducers is impractical and can corrupt the measurement by adding mass. Full-field, non-contact techniques can be used, such as Scanning Laser Doppler Vibrometry (SLDV) [1, 2], Holographic Interferometry [3], Electronic Speckle-Pattern Interferometry (ESPI) [4] and in the last decade, high-speed imaging, see, *e.g.*, Helfick *et al.* [5] and Wang *et al.* [6]. With high-speed imaging, Digital Image Correlation [7, 8], Gradient-Based methods (DIC) [9, 10] and Phase-Based methods [11, 12] are often used to identify the displacements. While the correlation accuracy is at the level of 1/100 of a pixel [13], for harmonic motion, much better amplitude accuracy can be achieved. With a hybrid method (camera + accelerometer) amplitudes of oscillation close to 1/100 000 of a pixel are possible [14, 15]. The use of high-speed imaging is also heavily researched for structural health monitoring [16, 17, 18].

Imaging methods are usually based on feature tracking on the structure, *e.g.*, line patterns [19, 20]. For the DIC algorithm, a speckle pattern with a high gradient in multiple directions is preferred [13]. That allows the displacement identification in the horizontal and vertical directions, as well as the rotation and deformation identification of the subset. For more details on the different pattern shapes and the methods for the identification of the pattern quality, see, *e.g.*, [21, 22].

In addition to pattern quality, the pattern application to the surface is also important. While the application method plays no role in the accuracy of the identified displacements (given equivalent pattern quality), it is; however, important from the surface preparation point of view. For different surface types, objects, and environments, different application methods are appropriate. Dong *et al.* [23] reviewed multiple application techniques, including airbrushing and spraying, spin coating, lithography, focused ion beam and scratching and abrading. In all cases, the surface of the object needed to be modified. This is not always possible and also not desirable where considerable amount of cleaning is needed to return the surface to it's original state or where the number of samples is large, *e.g.*, end-of-line control.

The interference pattern produced by the coherent light reflected from a rough surface [24] or by interference in the illuminating multi-mode optical fiber [25, 26] is usually an unwanted phenomenon in motion detection applications, for example vibrometry [27, 28], where a laser reflection from a moving target is interfered with the reference beam. The detected intensity change on the photodetector is directly related to the target translation and therefore the speckle intensity fluctuation represents an unwanted noise. It was shown; however, that the interference can be successfully used to identify the sub-micron-scale surface textures [29]. Additionally, the laser-speckle displacement can be directly associated with the rigid displacement of the object: Martin *et al.* [30] researched small objects (up to a diameter of 600 μm) for displacement identification on different surfaces. Further, Takai *et al.* [31] showed that an object's displacement perpendicular to the illumination direction can be identified when a fiber-coupled argon laser is used as a speckle source. In [31] a light interference in the multi-mode fiber caused a speckle pattern that interacted with the surface under investigation and served for the displacement identification. For small objects, up to 30 mm, the full-field laser speckle was researched for static deformation identification at room [32, 33] and elevated temperatures [34, 35]. The use of the laser speckle in the current applications is limited to a small area (30 mm) and mainly static deformations of the observed surface are measured.

In this research, a non-contact, multi-mode, laser-speckle-based measurement method is introduced for the operating-deflection-shape identification of structures much larger then previously (*e.g.*, [30, 35]) and at frequencies in the range of kHz; this was possible with a special experimental setup, as presented later. The method is researched for rigid-body motion and for the identification of the deflection shapes of a relatively large, flat-surface body.

This manuscript is organized as follows. Section 2 presents the theoretical background with respect to the displacement identification and laser speckle-pattern formation. In Section 3 the proposed method is presented. In Section 4 the experimental validation on three experimental setups is researched and Section 5 draws the conclusions.

2. Theoretical background

2.1. Obtaining the frequency response function from image data

Digital Image Correlation (DIC) [36] is the best-known method for displacement identification using sequential images. DIC is based on an optimization procedure that employs the minimization of the difference between the image at a specific time and a reference image. Generally, the difference between the subsets (pixels surrounding the observed point) of pixels is minimized, rather then the difference between the entire images. To increase spatial resolution, the subsets can overlap; however, if the overlap is larger than one third of the subset size, the resolution does not improve further [37]. Different cost functions can be chosen [8, 36], *e.g.*, the sum of squared differences:

$$SSD = \sum \left(f(u, v) - g(\zeta(u, v, \mathbf{t}))\right)^2, \tag{1}$$

where f is the reference image, g is the current image, $\zeta(u, v, \mathbf{t})$ is a function that transforms the image at a specific time to the reference image and $\mathbf{t}$ is an array of a vertical and horizontal displacement. Different transformation functions $\zeta(u, v, \mathbf{t})$ can be used, a commonly used is the affine transformation, that includes rotation and distortion of the subset. A simplified and numerically more efficient transformation function is used in this research, where only rigid translations are identified:

$$\zeta(u, v, \mathbf{t}) = \left\{ \begin{array}{c} u + t_0 \\ v + t_1 \end{array} \right\}, \tag{2}$$

where:

$$\mathbf{t} = \left\{ \begin{array}{c} \Delta y \\ \Delta x \end{array} \right\} \tag{3}$$

Δx and Δy are the displacements of interest and are optimized during the procedure. To successfully identify the displacements, the intensity pattern on the surface must translate along with the observed object. The information on the image is discretized to the grid of pixels and an interpolation is performed to identify the non-integer displacements. While DIC is most known for displacement identification (and will also be used in this research), it is worth noting that for oscillatory motion at the sub-pixel level, the simplified optical flow method is significantly faster, while having comparable accuracy [10].

During a vibration measurement, the excitation force is measured to estimate the Frequency Response Function (FRF):

$$\hat{\mathbf{H}}_\mathbf{1} = \frac{\hat{\mathbf{S}}_{\mathrm{FX}}(\omega)}{\hat{\mathbf{S}}_{\mathrm{FF}}(\omega)}, \tag{4}$$

where $\hat{\mathbf{S}}_{\mathrm{FX}}(\omega)$ and $\hat{\mathbf{S}}_{\mathrm{FF}}(\omega)$ are the cross and auto-spectra estimates, respectively [38]. The subscript $_{\mathrm{FF}}$ refers to the auto-spectrum of the force measurement and the subscript $_{\mathrm{FX}}$ refers to cross-spectrum of the force and the response measurement. Here, only the $\hat{\mathbf{H}}_\mathbf{1}$ estimate is presented, as averaging of spectra will not be used in this research, making the $\hat{\mathbf{H}}_\mathbf{1}$ and $\hat{\mathbf{H}}_\mathbf{2}$ estimates identical. The measured spectra are arrays at a single frequency, since Single-Input Multiple-Output (SIMO) methodology is used in this research. The estimated FRF is therefore also an array, indicated by the bold font in Eq. (4).

Based on the measured FRFs the modal identification is used to estimate the natural frequencies, modal shapes and damping [39, 40]. Dedicated, full-field modal identification methods for high-speed imaging were researched [14, 41, 42, 43, 44]. In the scope of this research, only the force normalized responses of the structure at the specific frequency points will be observed. These responses do not represent the structure's modal shapes, but are referred to as operating deflection shapes [45].

2.2. Forming a laser speckle pattern

The laser speckle pattern in illumination applications is the result of an interference pattern that is formed when the coherent light is scattered from an optically rough surface and/or propagates in the multi-mode optical fiber [25]. The acquired phase difference, due to the rough surface or the fiber length, forms a random-looking pattern of bright and dark spots on a screen, called speckle. Two types of speckle pattern are distinguished, namely, the subjective and objective [46].

Fig. 1 shows the scheme of the laser speckle forming on the objective O and subjective S planes of the imaging path after the laser light is scattered from an optically rough surface. Fig. 1 also shows the typical subjective speckle pattern produced after the illumination of the rough aluminium surface with the laser light.

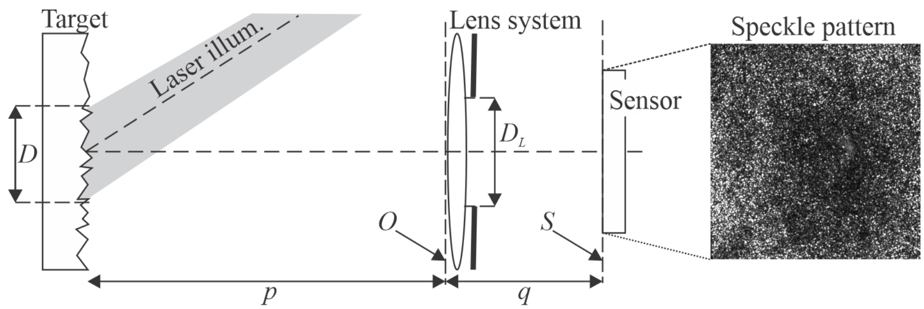

Figure 1: Illumination setup for the laser-speckles formation in the plane O for the objective pattern and in the plane S for the subjective pattern.

On one hand, when no lens system is used, the objective speckle pattern is formed. The laser light at wavelength λ is reflected from the surface area with the circular diameter D and average surface height variation d and falls on a screen or sensor at a distance p (plane O), see Fig. 1. The average objective speckle diameter is defined as [47]

$$\sigma_O = \frac{2.4\,\lambda\,p}{D} \tag{5}$$

On the other hand, when imaging the illuminated surface through a lens system, the subjective speckle pattern is formed. The lens system with aperture D_L is placed at distance p from the surface and the pattern is formed on the sensor at distance $p + q$, see Fig. 1. The subjective speckle diameter is defined by the diffraction and it holds that two spots cannot be distinguished, one from another, if the distance between them is less than σ_S:

$$\sigma_S = \frac{2.4\,\lambda\,q}{D_L} \tag{6}$$

The distance σ_S can also be expressed as:

$$\sigma_S = 2.4\,(1 + M)\,\lambda\,f_\#, \tag{7}$$

where M is the magnification of the lens system and $f_\#$ is the aperture number defined as:

$$f_\# = \frac{f}{D_L}, \tag{8}$$

where f is the focal length of the system. The subjective speckle is therefore always present when a lens system is used and is, in most cases, dominant. By reducing the size of the subjective speckle (its size depends on the chosen aperture number and magnification, as seen in Eq. (7)), the dominance of objective speckle is achieved in this research.

For DIC-based displacement identification, a high gradient (*i.e.*, contrast) in the speckle pattern is required. The contrast C of the speckles, generated using the laser light with the central wavelength λ and bandwidth $\Delta\lambda$, is proportional to [48]:

$$C \propto \left(2d\,\frac{\Delta\lambda}{\lambda^2}\right)^{-\frac{1}{2}} \tag{9}$$

The spectrum bandwidth $\Delta\lambda$ must be narrow enough for the speckle to be well defined and have a high contrast. This is not difficult to achieve when working with a single-mode illumination laser source, as the full-width at half-maximum (FWHM) of the emitted light spectrum is well below 1 nm. On the other hand, using multi-mode laser diodes, where the output spectrum can change and move with the driving current and its FWHM can exceed 3 nm, the spectral characteristic of the multi-mode light must be carefully controlled to achieve a speckle pattern with good contrast.

3. Laser-speckle formation for a relatively large area

In developing a full-field optical method for identifying the deflection shapes we must take into account several factors: speckle size, speckle contrast, speckle stability and the size of the illuminated field. The speckle size on the camera sensor, larger than the size of a sensor pixel, is crucial for accurate displacement identification [13]. The speckle size significantly depends on the aperture of the camera's lens system. The most common type is the subjective speckle and it works well in displacement identification [35] on a small observed region (typically 25 mm in diameter) and for cameras with small pixel sizes (typical 6 μm). For example, using Eq. (7) with a generic objective with a fixed focal length of f=50 mm, an illuminating wavelength of λ=976 nm and a magnification of M=0.2, we can calculate that the average speckle size is greater than σ_S=8 μm for apertures as large as 17 mm (f-number of f/2.8). From this example it is clear that subjective speckles larger than the pixel size can be achieved with relatively large apertures and consequently more light is transmitted to the sensor.

The method of using the subjective speckle conceptualized according to

Fig. 1 is used in this research to verify the displacement measurement of the aluminum plate (small observed region of 20 mm×20 mm) and an industrial camera (Basler A102f) with a pixel size of 6.45 μm, additionally, a high-speed camera (Photron FastCam SA-Z) with a pixel size of 20 μm was researched. For an experiment using a larger observed region (250 mm×250 mm) with a high-speed camera and a camera objective (AF-S VR Micro-Nikkor 105mm f/2.8G) the calculation of the subjective speckle size and the transmitted optical power is shown in Fig. 2. It is clear that with a decreasing aperture size the subjective speckle size σ_S increases; at the size of the pixel, the transmitted power falls to less than 20 %. Combining the low transmitted

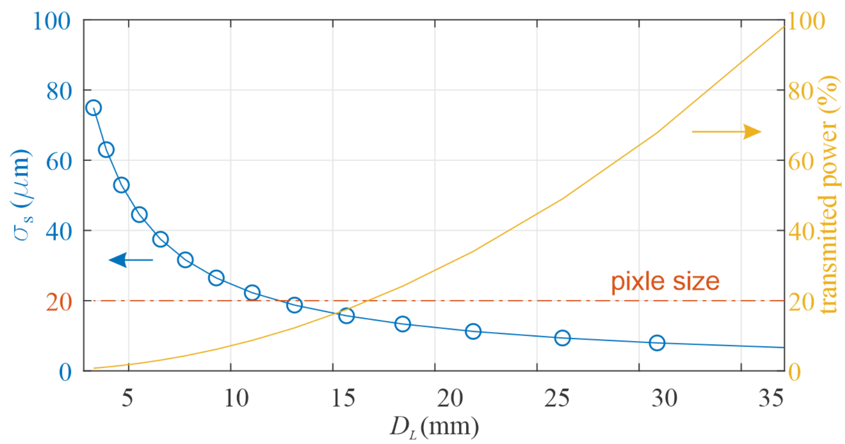

Figure 2: Subjective speckle size σ_S (left axis) and transmitted power (right axis) with the dependence on the lens aperture D_L

power with the short exposure times (less then 100 μs) a limit is achieved for the size of the illuminated field that can be observed and still have well-defined, large subjective speckles with good contrast. To some extent this can be addressed with an increase in the laser-illumination power.

To overcome the speckle-size / laser-power limitations, this research introduces the high-power, fiber-coupled, multi-mode, laser-diodes approach. The multi-mode laser sources are normally used for pumping fiber lasers and offer high reliability and have the potential to be used in direct industrial applications. Typical powers per module start at 10 W and can be found in compact packages up to 400 W. Further, the power scaling can be achieved by using fiber laser components such as fiber combiners that make possible combining the outputs of several laser diodes in a single fiber channel.

In the proposed laser illumination, a fiber coupled multi-mode laser diode with a nominal output power of 30 W at λ=976 nm and a spectral bandwidth under $\Delta\lambda$ =3 nm (II-VI, BMU30) was spliced to the larger double clad delivery fiber with a numerical aperture of NA=0.44. The larger fiber could in practice allow for the coupling of several 30 W modules in order to increase the illumination power, but for the proof of concept the method was tested with a single module up to 30 W of power for the larger observed region.

Another benefit of using the fiber-coupled laser source with a narrow spectral bandwidth is the formation of the speckles at the guiding fibre output and projecting such light onto the inspected surface where the interference pattern forms objective speckles. The concept of using objective speckles for a displacement measurement is shown in Fig. 3, where I is the illumination plane and L_1 marks the collimating lens that collects the light onto the desired region. In this configuration the imaging lens aperture D_L must be large enough so that, according to the Fig. 2, the size of the subjective speckles fall under the pixel size of the camera (20 μm for the Photron FastCam SA-Z).

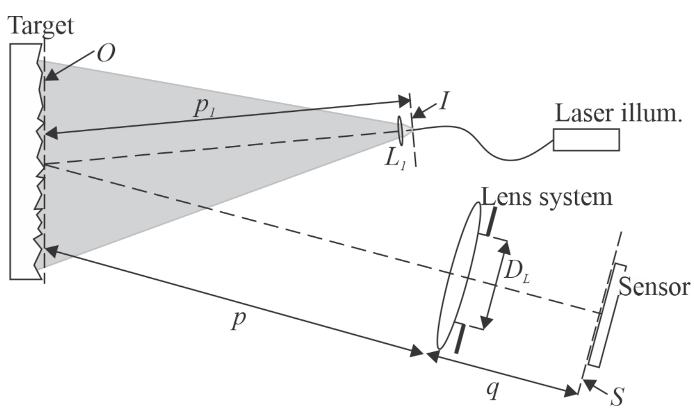

Figure 3: Setup for large field-of-view measurement employing objective speckles.

Using Eq. (5), the average size of the speckle on the object is 4 mm (wavelength λ =976 nm, p_1 = 45 cm and fiber diameter of 125 μm imaged by lens L_1 to diameter D=250 μm). This result is comparable to the experiment shown in Fig. 4b. Fig. 4 is showing the comparison of the objective and subjective speckle setups for the large observed region (250 mm$\times$250 mm). The validation of the objective speckles shown in Fig. 4b for the displacement identification is shown in Sec. 4.3. The poor contrast of the objective speckle in Fig. 4b is a consequence of a low surface height variation of the cymbal (smooth surface) and a larger laser-light bandwidth (larger than 1 nm) that was used to provide enough light reaching the camera sensor.

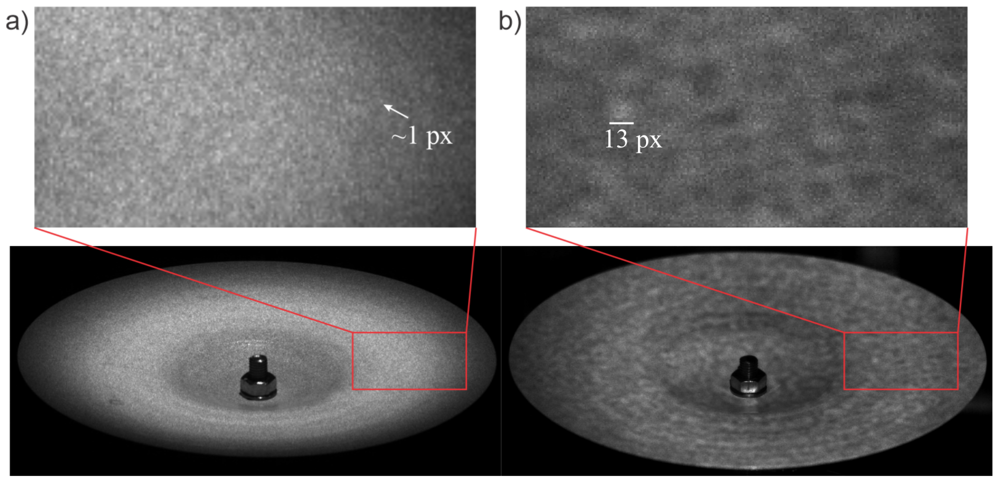

Figure 4: Comparison of a a) subjective and b) objective speckle size. Size of a speckle is indicated on a) and b).

In addition to the large observed region (large illumination field) a further requirement for the high-power illumination comes from the alignment of the measuring setup in a way that the direct reflection is eliminated and only the diffuse reflection forms the speckle-pattern on the sensor. Eliminating the direct reflection helps to avoid the local saturation of the image (where the speckles are consequently not visible) and provides the uniformity of the illuminated field when inspecting the curved and machined surfaces. This is especially true for the latter, which can have larger periodic surface features in addition to the smaller surface imperfections that are needed to form distinguishable, localized speckle pattern. The large periodic structures behave like the grating, forming a dominating interference pattern in a line perpendicular to the period of the structures with the intensity much larger than the speckle pattern from the whole surface. The difference is usually so large that the camera is locally saturated, which results in a loss of the movement-identification capability. For this reason the laser illumination, the camera and the inspected surface in the experiments are positioned in a way that eliminates direct reflection (the local or global saturation of the image is not present). Thus a homogeneous speckle pattern on complex surfaces is achieved at a cost of less optical power reaching the camera's sensor.

4. Experimental research

To validate the proposed method, three experiments were conducted. First, a linear displacement of a small object was observed and images were taken after each incremental displacement to validate the identification of the linear translation. Second, a high-speed camera was used to identify the rigid translations of the object mounted on an electrodynamic shaker, to validate the method for harmonic-motion identification. Third, the method was researched on a larger, flexible structure to test the validity of the method for full-field operating-deflection-shape identification on a relatively large scale.

4.1. Experiment 1: sequential images of linear displacement

An aluminium plate with a face of 20 mm×20 mm was used in the experiment (Fig. 5). The plate was mounted on a Thorlabs MAX300 positioning table and was moved horizontally by various increments in the range from 5 μm to 100 μm. A Basler A102f camera was used to record sequential images of the plate's surface illuminated by multi-mode laser with a central wavelength λ=915 nm and a nominal bandwidth $\Delta\lambda$=3 nm. Due to the camera having an objective with a focal length of f=50 mm and a maximum aperture of D_L=18 mm subjective speckles were dominant in the displacement identification. Twenty-five different subsets (51 px×51 px) were generated in a grid pattern, where the grid step was determined by the subset size. Their centre points are indicated in Fig. 5. The displacements were identified for all subsets using the DIC algorithm, implemented in an open-source pyIDI python package [49], where only rigid translations were tracked (2). In addition to observing the milled aluminium surface, a grade-200 and grade-800 abrading paper were used to randomize the surface pattern, resulting in approximate arithmetic average roughness profiles (R_a) of 30 μm and 10 μm, respectively. Abrading was used to compare the influence of surface roughness on displacement identification using laser-formed speckle pattern. The average speckle size was 35 μm, the size of a pixel on the camera sensor was 6.45 μm and the magnification was M=0.23.

To convert the identified displacements from pixels to meters, a known distance on the image was measured in pixels and was used to compute the size of a single pixel. To calibrate any further displacements that were in pixels, the displacement was multiplied with the size of a pixel. This

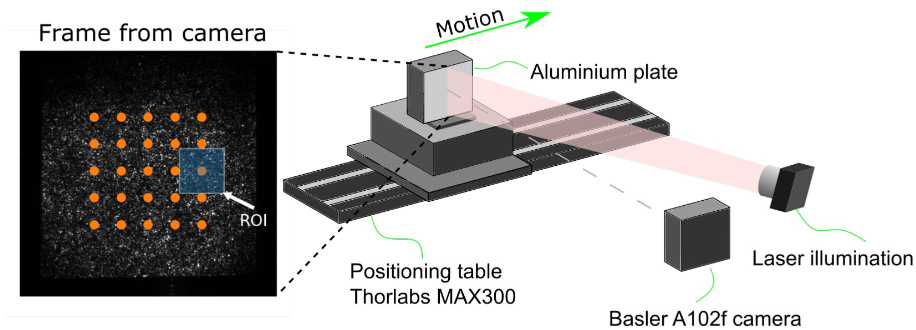

Figure 5: Experimental setup with positioning table.

can only be done under the assumption that the observed displacements are perpendicular to the optical axis of the camera and that the difference in scale (size of a pixel) between different points on the surface is negligible. This assumption was made for all three experiments in this research.

The identified displacements for all 25 points (Fig. 5) and for three different surfaces are plotted against the true displacements in Fig. 6. The standard deviation of the measurements at each position is presented on the secondary y-axis. It can be seen that the relationship between the identified and the true displacements is linear, the linear approximations (orange line in Fig. 6) having slopes of 1.0068, 1.00386 and 0.9967 for Figs. 6a, 6b and 6c, respectively. If different surfaces are compared, then the average standard deviation of the measurement scatter was 0.69 μm, 0.62 μm, 0.82 μm, for the milled, 200-grade-abraded and 800-grade-abraded surfaces, respectively. The largest error, found for the smoothest surface, can be attributed to the non-diffuse reflection of the laser light, which causes local saturation on the sensor, for details see Sec. 3. It is worth noting that, when sequential displacements are relatively small, the final displacement amplitude is not a limiting factor, as long as the laser-illumination conditions of the observed area remain constant.

4.2. Experiment 2: harmonic excitation

In this experiment the 200-grade-abraded aluminium plate (20 mm×20 mm) from experiment 1 was attached to the PCB CAL 200 electrodynamic shaker/calibrator, see Fig. 7. The calibrator has a built-in reference accelerometer that serves for the closed-loop control. A Photron FastCam SA-Z at 10 000 frames per second was used for the image acquisition. Again, the multi-mode laser illumination source was used (λ=915 nm, $\Delta\lambda$=3 nm). The aperture of the

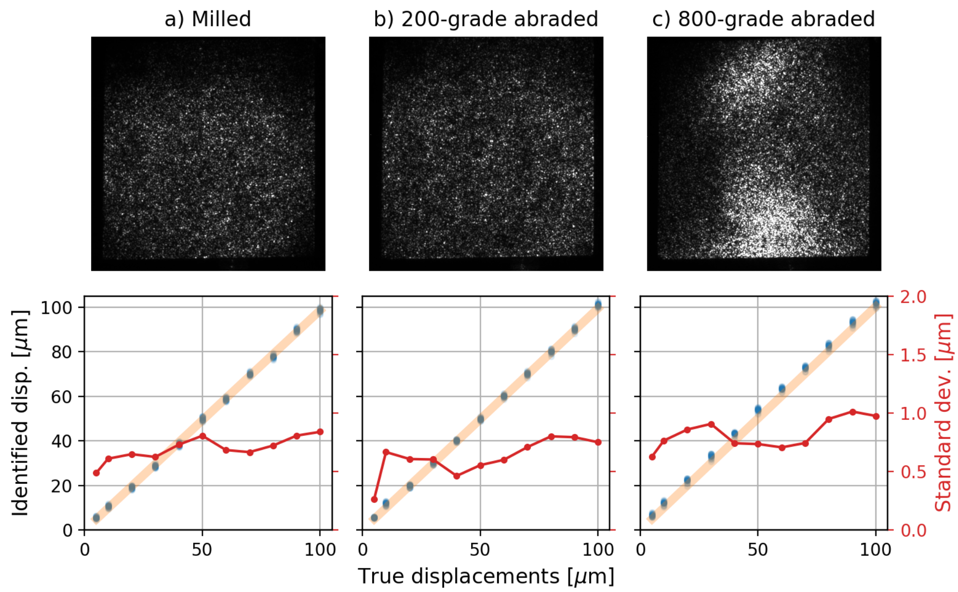

Figure 6: Identified displacements with respect to the true displacements (blue dots) and the standard deviation of the displacements on the secondary y-axis (red) for three different surfaces (top image).

camera's objective (AF-S VR Micro-Nikkor 105mm f/2.8G) was closed, so that the subjective speckles were dominant. The average speckle size on the camera sensor was 64 μm, the pixel size was 20 μm and the magnification was M=0.6.

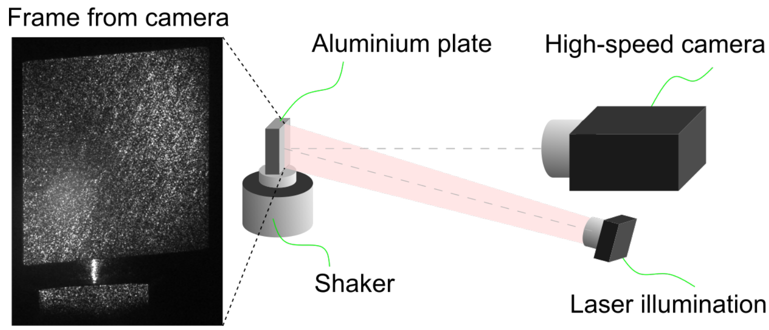

Figure 7: Experimental setup.

At the excitation frequency of 560 Hz, three sets of measurements at amplitudes 0.16 μm, 2.5 μm and 5 μm were made. An additional measurement at 230 Hz and amplitude of 15 μm was made, to inspect the relatively larger displacements. For each measurement, the displacements of 25 subsets (Fig. 5) were identified in order to confirm the rigid movement of the plate (2) [49]. As shown in Fig. 8, an increase in the excitation amplitude resulted in a linear increase in the response amplitude. The amplitude was computed using the frequency-domain approach, since the lower-frequency components in the signals would make the time-domain approach difficult. From the figure, it is clear that all the measured locations have the same response amplitude (variation can be seen in the magnified part of Fig. 8). The slope of the approximation line indicates the scaling of the amplitude, which is 33 μm/pixel.

Additionally, different excitation frequencies of 230 Hz and 560 Hz were tested at the excitation amplitude of 5 μm. Since the excitation frequencies are well below the first natural frequency (approximately 53 kHz) of the plate, the plate behaves as a rigid body. The response should not significantly depend on the excitation frequency. In Tab. 1, experimental results are listed: the standard deviation between 25 measurement locations at 230 Hz and 560 Hz is 0.0010 px and 0.0015 px. The mean amplitude of the displacement of the measured locations differs by approximately 2 % between the two excitation frequencies, which is within the limits of repeatability of the

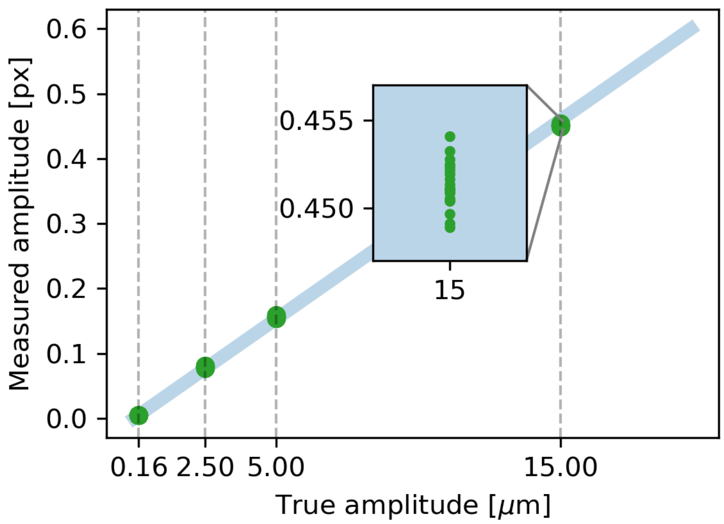

Figure 8: Response amplitude with respect to the excitation amplitude. Excitation frequency of 560 Hz was used with amplitudes 0.16 μm, 2.5 μm and 5 μm, 230 Hz with an amplitude of 15 μm.

measurement.

The time series of the identified displacements are shown in Fig. 9. All the displacements are shown for the same observed point on the image.

Table 1: Response amplitude and standard deviation at different frequencies with an excitation amplitude of 5 μm.

Exc. frequency [Hz]	Mean meas. amp.	Meas. amp. STD
230	0.1534 px / 5.00 μm	0.0010 px / 0.049 μm
560	0.1565 px / 5.09 μm	0.0015 px / 0.034 μm

4.3. Experiment 3: Full-field vibration measurement

To research the proposed method for a relatively large object vibration measurement, a 250-mm-diameter cymbal was used; in previous research [10] a similar cymbal was used with a classic sprayed speckle pattern and the modal shapes were successfully extracted using the high-speed camera measurement.

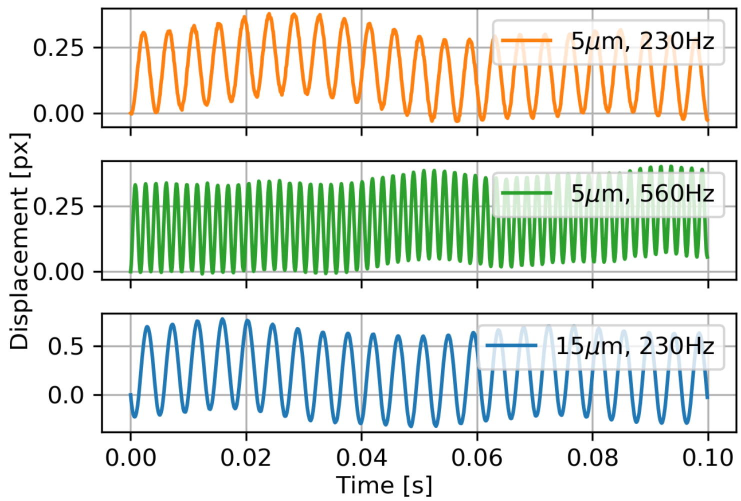

Figure 9: Identified displacements at different amplitudes and excitation frequencies.

The experimental setup is shown in Figs. 10 and 11. Two displacement measurements were performed: firstly, with the laser-pattern and secondly, after the black speckles were sprayed, with LED lights illuminating the surface. The two illumination sources are shown in Fig. 11 (A - LED lights and B - laser illumination) and were not used simultaneously; before the experiments, the cymbal was painted white (due to the similar mass loading). Due to surface preparation, the cymbal was detached, which caused slight orientation difference between laser and paint speckle experiment.

The cymbal was attached to the LDS V406 electrodynamic shaker. To measure the force of excitation, a PCB 208C01 force transducer was inserted between the shaker and the cymbal. A Photron FastCam SA-Z high-speed camera was used. The angle of the camera's optical axis with respect to the cymbal plain was approximately 30°, while the video was captured at 20 000 FPS for an image size 1024 px×512 px. Using this experimental setup, only the projections of the displacements to the camera plane were measured, providing 2D displacements, only. Frequency-domain triangulation could be used to obtain the 3D responses [50].

As discussed in Sec. 3, on a larger object an appropriate subjective speckle pattern is difficult to form and then retain enough intensity. According to Fig. 2, the aperture of the camera D_L was enlarged, to have enough intensity on the detector. As a consequence, the sizes of the subjective speckles were

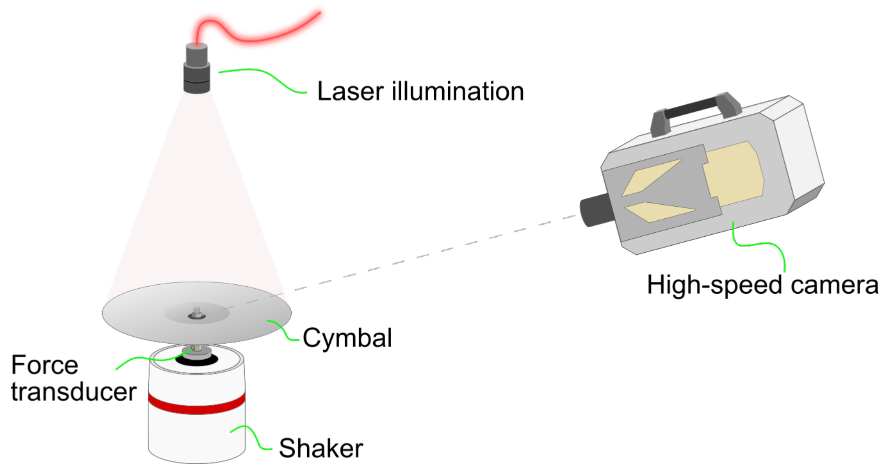

Figure 10: Cymbal experiment set-up (laser-speckle).

much less than one camera pixel in diameter (speckle size was 8 μm and camera pixel size was 20 μm). For this reason, the objective speckle was used, with the average diameter on the camera's sensor being 2.4 mm. An assembly consisting of a lens with a focal length of 40 mm was used and the output from an illuminating fiber was projected on the cymbal surface.

Both the laser-speckle and the classic paint-speckle displacement identifications were based on a 2-second-long high-speed video; the displacements were identified in roughly 17 000 subsets (81 px$\times$81 px) using DIC [49]; the centers of subsets are shown in Fig. 12.

Prior to deflection shape measurement, the cymbal was excited at two discrete frequencies to validate the use of objective speckle. A 1-second harmonic excitation (72.4 Hz and 144.8 Hz) of the cymbal was performed and the displacements were identified based on the objective speckle pattern for the location marked with orange in Fig. 12. The response of the cymbal is shown in Figs. 13a and 14a for both excitation frequencies. From the frequency-domain representation it can be seen that the dominant peaks occur at the excitation frequency, see Fig. 13b and 14b. Due to the proximity of the first natural frequency (at approx. 115 Hz) the motion of the cymbal at selected frequencies is far from rigid. The objective speckle used in the cymbal measurement is presented in Fig. 15, showing two positions of the cymbal during a sine excitation. The position shown in Fig. 15b is chosen at the maximum negative displacement, while Fig. 15c is chosen at the maximum positive displacement. The maximum range of displacements

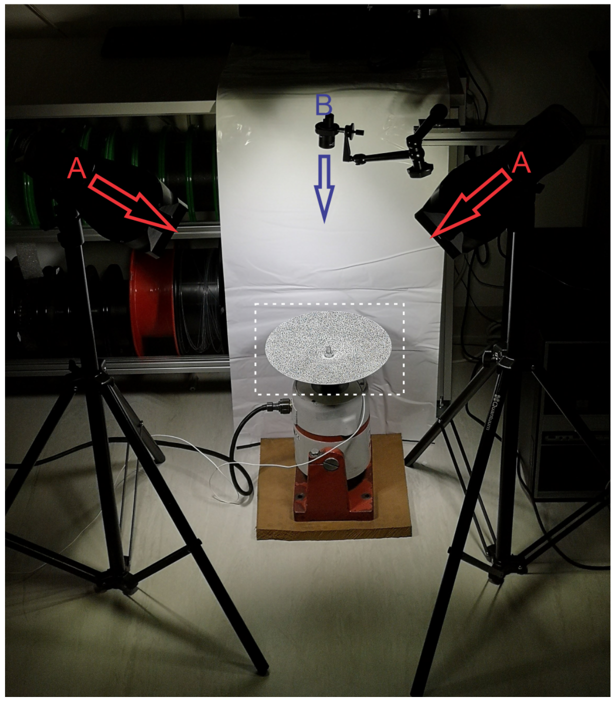

Figure 11: Experiment set-up. A - LED lights and B - laser illumination.

was not evaluated in detail, typical values for correlation distance in such experiments; however, are on the scale of several millimetres [31].

To identify the full-field operating-deflection-shapes, the cymbal was excited with a 2-second-long logarithmic sine-sweep from 50 Hz to 3000 Hz (approx. 3 octave/sec) with a constant amplitude.

As the triggering of the camera and the force measurement was not synchronized on the same data-acquisition system, time shifting was used during the post-processing of the recorded data in order to align the phase information. A trigger was used to detect the start of excitation. The delay between the camera and force measurement was used to time-shift the signals in the frequency domain [51]. After the DIC identification, the camera-based displacements were used with the force information to estimate the FRFs (4) at close to 17 000 locations. No averaging was used in the FRF identification procedure. The obtained FRF for a single subset (marked in Fig. 12) is presented in Fig. 16. The amplitudes in the areas of the natural frequencies are similar for both measurements. The noise was characterized for the displacement measurement only, where no excitation was applied; the noise Root

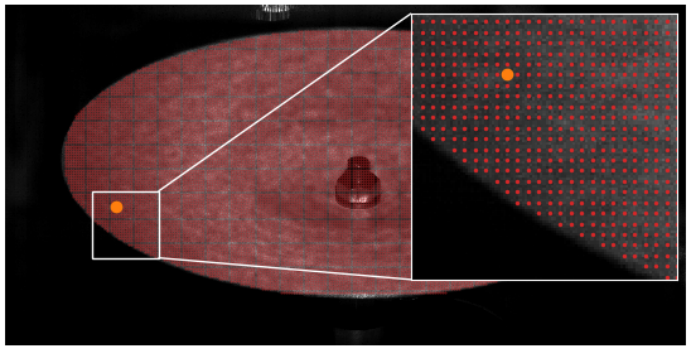

Figure 12: Centres of subsets used for the displacement identification.

Mean Square (RMS) was $2.17 \cdot 10^{-8}$ m and $3.06 \cdot 10^{-8}$ m for the paint and laser speckle, respectively. Additionally, some peaks are slightly frequency-shifted due to the non-identical experimental setup, a result of cymbal detachment for surface preparation and the cymbal itself not being identical due to the black spray paint.

From the FRFs, the natural frequencies and operational deflection shapes were identified (14 shapes were identified in the frequency range up to 1300 Hz). Additionally, a simplified, non-validated, numerical model of the cymbal was prepared in order to obtain numerical shapes for a comparison with the experimental data. Five representative deflection shapes, measured using laser speckle, paint speckle and the numerical simulations are shown in Fig. 17. As can be seen from the figure, the displacement identification of the laser-speckle measurement for full-field identification is of lower quality than the paint-speckle measurement. From the results it is clear that the quality depends on the location of the displacement identification and on the laser/camera reflection angle, *e.g.*, central area, where the cymbal is attached to the shaker.

To quantitatively describe the difference between the laser speckle and the paint speckle, the results of Fig. 17 were first aligned and the error was computed:

$$Err_i = \frac{|\phi_{\text{laser},i} - \phi_{\text{paint},i}|}{|\phi_{\text{paint},i}|} \cdot 100, \tag{10}$$

where $\phi_{\text{laser},i}$ is the ith laser-speckle shape and $\phi_{\text{paint},i}$ is the ith paint-speckle shape. Since the paint-speckle is considered to be the more established and

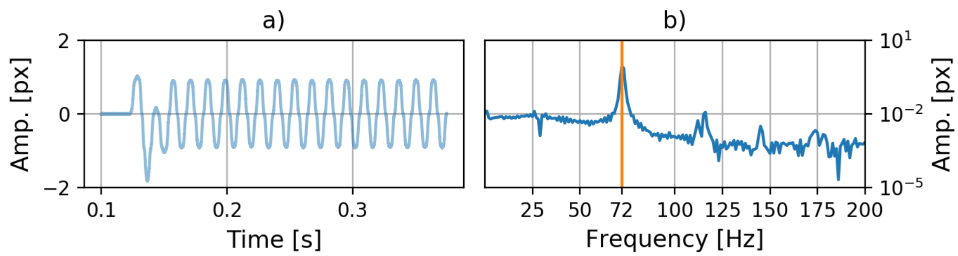

Figure 13: Identified response of the cymbal to sine excitation at 72.4 Hz. a) time domain and b) frequency domain.

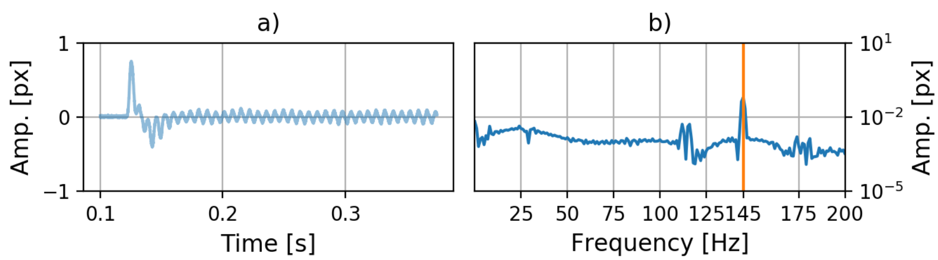

Figure 14: Identified response of the cymbal to sine excitation at 144.8 Hz. a) time domain and b) frequency domain.

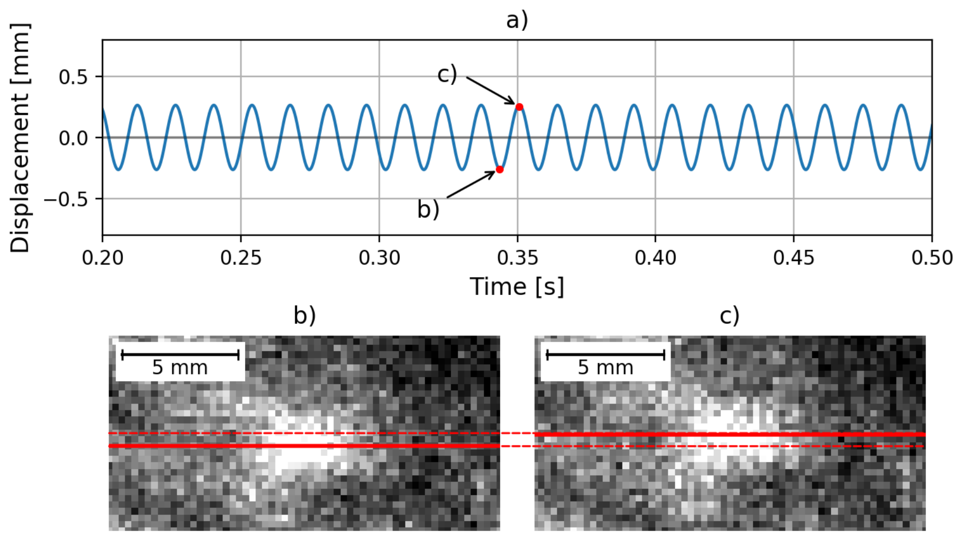

Figure 15: a) excitation signal and zoom in on the objective speckle in b) bottom and c) top position.

accurate technique, this was used as a measure of laser-speckle experiment quality. Fig. 18 shows the normalized error distribution across the cymbal for deflection shapes, where the problematic regions are most evident. The locations of large error are partially dependent on the observed deflection shape, but to the most part the large error region can be observed in the center of the cymbal. At the center of the cymbal the amplitudes of the vibration are small and therefore the noise floor of the laser speckle is exposed; additionally, in the central region the curvature of the cymbal is significantly

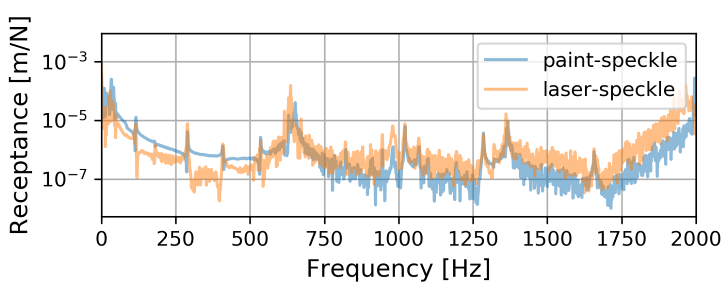

Figure 16: FRF obtained using LED and laser illumination.

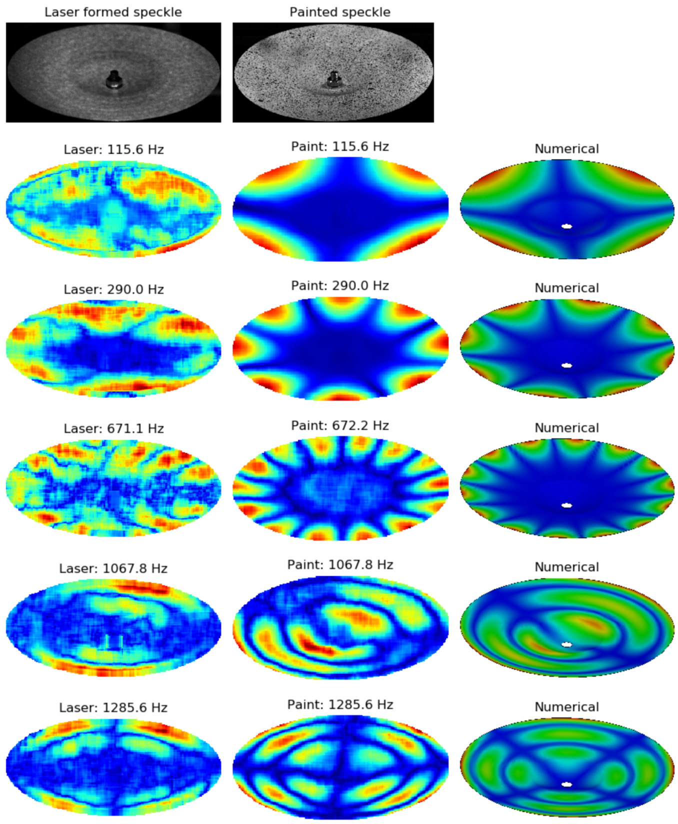

Figure 17: Comparison of deflection shapes for laser and paint speckle (color is in scale). Numerical results are shown as a reference (color not in scale).

different than elsewhere, which results in laser-light deflecting away from the camera or the reflection is not diffuse. An additional area of larger error can be observed on the right edge of the cymbal, where the laser illumination conditions (angle of the laser, light intensity, direct reflection) contribute to the error.

5. Conclusions

This study researches the use of laser speckle for the vibration measurements of relatively large structures (*e.g.*, diameter of approx. 250 mm). Compared to the normally used sprayed speckle pattern, the laser speckle promises to leave the observed surface untouched.

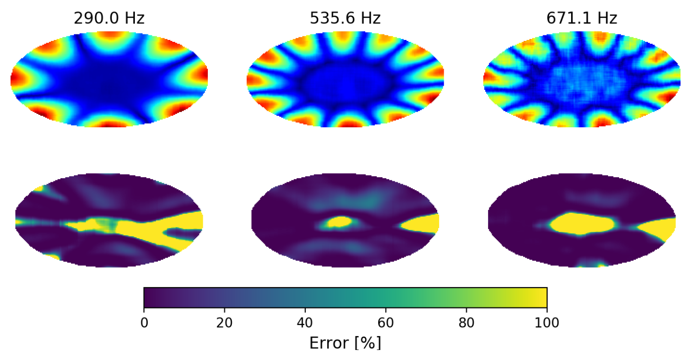

Figure 18: Deflection shapes from paint speckle experiment (top) and normalized error distribution of the laser and paint-speckle deflection shape (bottom).

The objective and subjective laser speckle, spectral properties of the multi-mode laser diodes, the laser power and the surface roughness were researched with respect to the speckle size and contrast for the digital-image-correlation displacement identification.

The accuracy of the laser speckle was experimentally researched with three experiments. The first experiment was a rigid-body experiment where micrometer displacements were researched using a linear positioning table. A small metallic plate ($20\,\text{mm}\times 20\,\text{mm}$) was observed, where a laser-speckle size above one pixel was achieved using a subjective speckle. Sequential displacements in range from 0 to $100\,\mu$m were identified for three different surface finishes. The difference between the real and the identified displacements was always better than 1%. The displacements for the 200-grade-abraded surface had the smallest standard deviation for the 25 observed locations ($0.62\,\mu$m on average), while the 800-grade-abraded surface had the largest standard deviation ($0.82\,\mu$m on average).

The second experiment was for rigid-body harmonic displacement identification. The same metallic plate as in the first experiment was attached to a shaker and researched for different excitation frequencies and amplitudes. For the two excitation frequencies (230 Hz and 560 Hz), the amplitudes differed by at most 2%, if compared to a reference measurement.

The third experiment was for a full-field deflection-shape measurement of a relatively large object ($250\,\text{mm}\times 250\,\text{mm}$). A sine-sweep was used on two parallel experiments, namely, laser speckle and paint speckle. The identified natural frequencies from both experiments were in agreement. If compared to the paint-speckle measurement, the laser-speckle approach was found to have a higher noise RMS ($2.17{\cdot}10^{-8}$ m for paint-speckle vs. $3.06{\cdot}10^{-8}$ m for laser-speckle approach); further, the optical setup of the experiment was found to significantly impact the measurement (*e.g.* due to non diffuse laser-light reflection). To enhance the identification of the operational shapes, further improvements of the method should be considered, such as: making the illumination system more stable, testing the light source at shorter wavelengths (less then 800 nm) to increase the sensitivity of the camera and improving the dynamic range of displacement identification by modifying the DIC algorithm to seek correlation frame-to-frame rather than frame-to-reference frame.

This research shows that the laser speckle is promising for full-field vibration analysis; however, for accurate measurements the noise floor needs to be carefully analysed and the experimental setup well prepared (especially the optical part).

Acknowledgements

The authors acknowledge the partial financial support from the Slovenian Research Agency (research projects J2-1730 and N2-0144).

References

[1] A B Stanbridge and D J Ewins. Modal Testing Using a Scanning Laser Doppler Vibrometer. *Mechanical Systems and Signal Processing*, 13(2):255–270, 1999.

[2] David A Ehrhardt, Matthew S Allen, Shifei Yang, and Timothy J Beberniss. Full-field linear and nonlinear measurements using Continuous-Scan Laser Doppler Vibrometry and high speed Three-Dimensional Digital Image Correlation. *Mechanical Systems and Signal Processing*, 86:82–97, 2017.

[3] L O Heflinger, R F Wuerker, and R Eo Brooks. Holographic interferometry. *Journal of Applied Physics*, 37(2):642–649, 1966.

[4] Ole J Løkberg. Electronic speckle pattern interferometry. In *Optical metrology*, pages 542–572. Springer, 1987.

[5] Mark N Helfrick, Christopher Niezrecki, Peter Avitabile, and Timothy Schmidt. 3D digital image correlation methods for full-field vibration measurement. *Mechanical Systems and Signal Processing*, 25(3):917–927, 2011.

[6] Weizhuo Wang, John E Mottershead, Thorsten Siebert, and Andrea Pipino. Frequency response functions of shape features from full-field vibration measurements using digital image correlation. *Mechanical Systems and Signal Processing*, 28:333–347, 2012.

[7] W. H. Peters and W. F. Ranson. Digital Imaging Techniques In Experimental Stress Analysis. *Optical Engineering*, 21(3):213427, jun 1982.

[8] Bing Pan. Digital image correlation for surface deformation measurement: historical developments, recent advances and future goals. *Measurement Science and Technology*, 29(8):82001, 2018.

[9] Bruce D Lucas and Takeo Kanade. An Iterative Image Registration Technique with an Application to Stereo Vision. In *Proceedings of the 7th International Joint Conference on Artificial Intelligence - Volume 2*, IJCAI'81, pages 674–679, San Francisco, CA, USA, 1981. Morgan Kaufmann Publishers Inc.

[10] Jaka Javh, Janko Slavič, and Miha Boltežar. The subpixel resolution of optical-flow-based modal analysis. *Mechanical Systems and Signal Processing*, 88:89–99, 2017.

[11] David J Fleet and Allan D Jepson. Computation of component image velocity from local phase information. *International journal of computer vision*, 5(1):77–104, 1990.

[12] Aral Sarrafi, Zhu Mao, Christopher Niezrecki, and Peyman Poozesh. Vibration-based damage detection in wind turbine blades using Phase-based Motion Estimation and motion magnification. *Journal of Sound and vibration*, 421:300–318, 2018.

[13] Rafael C Gonzalez, Richard E Woods, and Steven L Eddins. *Digital Image Processing Using MATLAB*. Prentice-Hall, Inc., USA, 2003.

[14] Jaka Javh, Janko Slavič, and Miha Boltežar. High frequency modal identification on noisy high-speed camera data. *Mechanical Systems and Signal Processing*, 98:344–351, 2018.

[15] Tomaž Bregar, Klemen Zaletelj, Gregor Čepon, Janko Slavič, and Miha Boltežar. Full-field FRFs estimation from noisy high-speed camera data using dynamic substructuring approach. *Mechanical Systems and Signal Processing*, 2021. in press.

[16] Junhwa Lee, Kyoung-Chan Lee, Seunghoo Jeong, Young-Joo Lee, and Sung-Han Sim. Long-term displacement measurement of full-scale bridges using camera ego-motion compensation. *Mechanical Systems and Signal Processing*, 140:106651, 2020.

[17] HweeKwon Jung, Andre Green, John Morales, Moises Silva, Bridget Martinez, Alessandro Cattaneo, Yongchao Yang, Gyuhae Park, Jarrod McClean, and David Mascareñas. A holistic cyber-physical security protocol for authenticating the provenance and integrity of structural health monitoring imagery data. *Structural Health Monitoring*, page 1475921720927323, 2020.

[18] Chuan-Zhi Dong and F Necati Catbas. A review of computer vision–based structural health monitoring at local and global levels. *Structural Health Monitoring*, page 1475921720935585, 2020.

[19] Sutanu Bhowmick, Satish Nagarajaiah, and Zhilu Lai. Measurement of full-field displacement time history of a vibrating continuous edge from video. *Mechanical Systems and Signal Processing*, 144:106847, 2020.

[20] Tengjiao Jiang, Gunnstein Thomas Frøseth, Anders Rønnquist, and Egil Fagerholt. A robust line-tracking photogrammetry method for uplift measurements of railway catenary systems in noisy backgrounds. *Mechanical Systems and Signal Processing*, 144:106888, 2020.

[21] D Lecompte, ASHJD Smits, Sven Bossuyt, Hugo Sol, J Vantomme, D Van Hemelrijck, and A M Habraken. Quality assessment of speckle patterns for digital image correlation. *Optics and lasers in Engineering*, 44(11):1132–1145, 2006.

[22] Bing Pan, Zixing Lu, and Huimin Xie. Mean intensity gradient: An effective global parameter for quality assessment of the speckle patterns

used in digital image correlation. *Optics and Lasers in Engineering*, 48(4):469–477, 2010.

[23] Y L Dong and B Pan. A review of speckle pattern fabrication and assessment for digital image correlation. *Experimental Mechanics*, 57(8):1161–1181, 2017.

[24] KA O'Donnell and ER Mendez. Experimental study of scattering from characterized random surfaces. *JOSA A*, 4(7):1194–1205, 1987.

[25] Donatus Halpaap, Jordi Tiana-Alsina, Meritxell Vilaseca, and Cristina Masoller. Experimental characterization of the speckle pattern at the output of a multimode optical fiber. *Optics express*, 27(20):27737–27744, 2019.

[26] DZ Anderson, MA Bolshtyansky, and B Ya Zel'dovich. Stabilization of the speckle pattern of a multimode fiber undergoing bending. *Optics letters*, 21(11):785–787, 1996.

[27] Steve Rothberg. Numerical simulation of speckle noise in laser vibrometry. *Applied Optics*, 45(19):4523–4533, 2006.

[28] Peter Martin and Steve Rothberg. Introducing speckle noise maps for laser vibrometry. *Optics and Lasers in Engineering*, 47(3-4):431–442, 2009.

[29] Motochika Shimizu, Hiroshi Sawano, Hayato Yoshioka, and Hidenori Shinno. Multi-dimensional assessment of nano/micro scale surface texture using laser speckle pattern analysis. *Journal of Advanced Mechanical Design, Systems, and Manufacturing*, 9(1):JAMDSM0011–JAMDSM0011, 2015.

[30] Peter Martin and Steve Rothberg. Laser vibrometry and the secret life of speckle patterns. In *Eighth International Conference on Vibration Measurements by Laser Techniques: Advances and Applications*, volume 7098, page 709812. International Society for Optics and Photonics, 2008.

[31] Nobukatsu Takai and Toshimitsu Asakura. Laser speckles produced by a diffuse object under illumination from a multimode optical fiber: an experimental study. *Applied optics*, 27(3):557–562, 1988.

[32] Jinlian Song, Jianhong Yang, Fujia Liu, and Kefei Lu. High temperature strain measurement method by combining digital image correlation of laser speckle and improved ransac smoothing algorithm. *Optics and Lasers in Engineering*, 111:8–18, 2018.

[33] N Mashiwa, T Furushima, and K Manabe. Novel non-contact evaluation of strain distribution using digital image correlation with laser speckle pattern of low carbon steel sheet. *Procedia Engineering*, 184:16–21, 2017.

[34] Qiu Zheng, Naoki Mashiwa, and Tsuyoshi Furushima. Evaluation of large plastic deformation for metals by a non-contacting technique using digital image correlation with laser speckles. *Materials & Design*, page 108626, 2020.

[35] Marcus Anwander, Bernhard G Zagar, Brigitte Weiss, and H Weiss. Noncontacting strain measurements at high temperatures by the digital laser speckle technique. *Experimental mechanics*, 40(1):98–105, 2000.

[36] B Pan, K Li, and W Tong. Fast, Robust and Accurate Digital Image Correlation Calculation Without Redundant Computations. *Experimental Mechanics*, 53(7):1277–1289, sep 2013.

[37] Elizabeth MC Jones, Mark A Iadicola, et al. A good practices guide for digital image correlation. *International Digital Image Correlation Society*, 10, 2018.

[38] Zhi-Fang Fu and Jimin He. *Modal analysis*. Elsevier, 2001.

[39] Nuno Manuel Mendes Maia and Júlio Martins Montalvao e Silva. *Theoretical and experimental modal analysis*. Research Studies Press, 1997.

[40] Klemen Zaletelj, Tomaž Bregar, Domen Gorjup, and Janko Slavič. ladisk/pyema: v0.24, September 2020.

[41] Yongchao Yang and Charles Dorn. Affinity propagation clustering of full-field, high-spatial-dimensional measurements for robust output-only modal identification: A proof-of-concept study. *Journal of Sound and Vibration*, page 115473, 2020.

[42] Zonghui Chen, Wen Xiao, Feng Pan, Hongliang Hao, and Lan Ma. Modal analysis using camera-based heterodyne interferometry and

acoustic excitation. *Mechanical Systems and Signal Processing*, 128:295–304, 2019.

[43] Moisés Silva, Bridget Martinez, Eloi Figueiredo, João CWA Costa, Yongchao Yang, and David Mascareñas. Nonnegative matrix factorization-based blind source separation for full-field and high-resolution modal identification from video. *Journal of Sound and Vibration*, 487:115586, 2020.

[44] Yunus Emre Harmanci, Utku Gülan, Markus Holzner, and Eleni Chatzi. A novel approach for 3d-structural identification through video recording: magnified tracking. *Sensors*, 19(5):1229, 2019.

[45] Patrick L McHargue and Mark H Richardson. Operating Deflection Shapes From Time Versus Frequency Domain Measurements. *Imac Xi*, pages 1–8, 1993.

[46] J Christopher Dainty. *Laser speckle and related phenomena*, volume 9. Springer science & business Media, 2013.

[47] Mikael Sjödahl and LR Benckert. Systematic and random errors in electronic speckle photography. *Applied Optics*, 33(31):7461–7471, 1994.

[48] Jeffrey G Manni and Joseph W Goodman. Versatile method for achieving 1% speckle contrast in large-venue laser projection displays using a stationary multimode optical fiber. *Optics express*, 20(10):11288–11315, 2012.

[49] Klemen Zaletelj, Domen Gorjup, and Janko Slavič. ladisk/pyidi: Release of the version v0.23, September 2020.

[50] D. Gorjup, J. Slavič, and Miha Boltežar. Frequency domain triangulation for full-field 3D operating-deflection-shape identification. *Mechanical Systems and Signal Processing*, 133, 2019.

[51] Kihong Shin and Joseph Hammond. *Fundamentals of signal processing for sound and vibration engineers*. John Wiley & Sons, 2008.